

## Budding of crystalline domains in fluid membranes

T. Kohyama,<sup>1,\*</sup> D. M. Kroll,<sup>2</sup> and G. Gompper<sup>1</sup>

<sup>1</sup>*Institut für Festkörperforschung, Forschungszentrum Jülich, D-52425 Jülich, Germany*

<sup>2</sup>*Supercomputing Institute, University of Minnesota, 599 Walter Library, 117 Pleasant Street S.E., Minneapolis, Minnesota 55455, USA*

(Received 25 July 2003; published 17 December 2003)

Crystalline domains embedded in fluid membrane vesicles are studied by Monte Carlo simulations of dynamically triangulated surfaces and by scaling arguments. A budding transition from a caplike state to a budded shape is observed for increasing spontaneous curvature  $C_0$  of the crystalline domain as well as increasing line tension  $\lambda$ . The location of the budding transition is determined as a function of  $C_0$ ,  $\lambda$ , and the radius  $R_A$  of the crystalline domain. In contrast to previous theoretical predictions, it is found that budding occurs at a value of the spontaneous curvature  $C_0$ , that is always a decreasing function of the domain size  $R_A$ . Several characteristic scaling regimes are predicted. The distribution of five- and sevenfold disclinations as the budding transition is approached is determined, and the dynamics of the generation of defects is studied.

DOI: 10.1103/PhysRevE.68.061905

PACS number(s): 87.16.Dg, 64.70.Dv, 82.70.-y

### I. INTRODUCTION

The primary new feature in two-component—compared to single-component—fluids is the possibility of phase separation. Canonically, mixtures have a lower miscibility gap, that is, the system is homogeneously mixed at high temperatures, but demixes at low temperatures into two coexisting phases that are enriched in one of the two components. However, upper miscibility gaps and closed coexistence loops also exist, typically in systems in which the hydrophobic effect is important. The inverted phase behavior of these systems is due to the orientational degrees of freedom of the water molecules, which are distributed isotropically at high temperatures, but have a preferred orientation in the neighborhood of polar solutes.

It is therefore natural to expect phase separation in two-component amphiphilic membranes. Indeed, phase separation in Langmuir monolayers at the water-air interface has been well documented for many years, and has been investigated in considerable detail [1,2]. However, in bilayer membranes, phase separation turns out to be much more difficult to observe. Initial evidence showed gel-fluid coexistence in some systems [3], while fluid-fluid coexistence remained elusive for a long time. Only very recently have experiments using three-component membranes revealed very clear and convincing evidence for both gel-fluid [4,5] and fluid-fluid [6,7] coexistence.

The coupling of phase separation and membrane shape in flexible bilayer membranes opens the possibility for the budding of domains [8,9]. The physical mechanism of this phenomenon is the competition between the line tension energy of the phase boundary and the curvature energy of the membrane. Since the curvature energy is scale invariant, so that the curvature energy of a spherical vesicle is independent of the vesicle radius, and the line tension energy is proportional to the domain perimeter, i.e., to the domain radius, it is immediately clear that a budding transition occurs when the

domain radius  $R$  is on the order of  $\kappa/\lambda$ , where  $\kappa$  is the bending rigidity and  $\lambda$  is the line tension. Similarly, a membrane patch with spontaneous curvature  $C_0$  has a budding transition at  $R \sim 1/C_0$ .

The coexistence of two phases in biological membranes has also received considerable attention recently. The existence of “lipid rafts” [10] may indeed play an important role in the control of the activity of membrane proteins. Another kind of two-phase coexistence in biological membranes occurs when domains of adsorbed proteins form spontaneously. A famous, and biologically very important, example is the adsorption of clathrin molecules on the plasma membrane [11]. Clathrin molecules assemble to form a regular hexagonal network on the membrane surface [12–14]. By forming first a coated pit and then a complete bud (see Fig. 1), these clathrin coats control endo- and exocytosis, i.e., the formation and detachment of small transport vesicles from the cell membrane. The formation of clathrin cages is therefore an example of the budding of crystalline membrane patches embedded in a fluid lipid membrane.

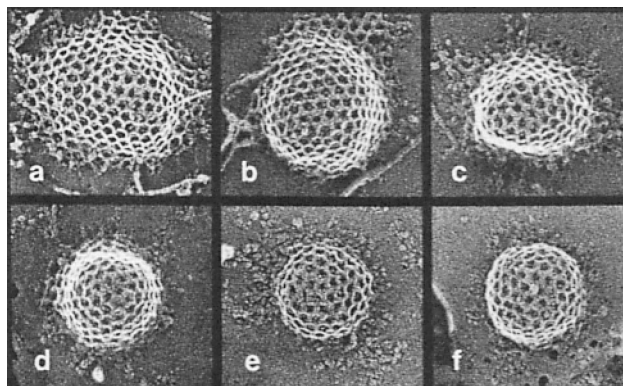


FIG. 1. Rounded clathrin-coated pits in normal chick fibroblasts (a)–(d) and coated pits on membrane fragments derived from cells that have been broken open and left in pH 7 buffer for 10 min at 25 °C before fixation and freeze drying (e)–(f). The width of the field of view of the individual pictures is 0.4  $\mu\text{m}$ . Reproduced from Ref. [14] by copyright permission of The Rockefeller University Press.

\*Permanent and present address: Department of Physics, Faculty of Education, Shiga University, Hiratsu 2-5-1, Otsu, Shiga 520-0862, Japan.

The main difference between a fluid and a crystalline membrane domain is the in-plane shear elasticity and positional long-range order of the crystalline phase. A flat, crystalline membrane cannot be deformed into a spherical bud without the introduction of topological defects. For the generic case of a hexagonal lattice symmetry, the crystal consists of a network of sixfold coordinated vertices. In this case, Euler's theorem requires an excess of exactly 12 fivefold coordinated vertices (or fivefold disclinations) to form a spherical cage. A disclination is a topological defect, because it cannot be generated locally, but requires the rearrangement of a large number of lattice sites. An important question, therefore, is how these fivefold disclinations are generated inside the crystalline domain. Two principal mechanisms are possible. In the first, the *edge-acquisition mechanism*, fivefold disclinations form at the edge of the crystalline domain and then diffuse into the interior [12]. Diffusion proceeds through the production of a series of dislocations, which consist of nearest-neighbor pairs of five- and sevenfold disclinations. In the second, the *interior-acquisition mechanism*, dislocation pairs are generated in the interior of the crystalline patch. Each of these dislocations subsequently dissociates, leaving the fivefold disclination in the interior of the patch while the sevenfold disclination diffuses to the domain boundary. Another possibility has been suggested for clathrin networks, in which fivefold coordinated sites are formed through the addition of clathrin dimers to the interior of clathrin domains [15].

The interior-acquisition mechanism has been studied in detail by Mashl and Bruinsma [16]. They argue that budding occurs via dislocation unbinding, driven by changes in the spontaneous curvature of the clathrin and associated lipid membrane assembly. Mashl and Bruinsma estimate the curvature and stretching energies of a fivefold disclination in the center the domain and a sevenfold disclination at distance  $r$ . With increasing  $C_0$ , the minimum of their free-energy ansatz was found to move to larger values of  $r$ , until  $r=R_A$  is reached at a critical value of the spontaneous curvature. This disclination unbinding allows the sevenfold disclination to move to the edge of the network, leaving behind the fivefold disclination at the center. In this approach, budding occurs for  $R \sim C_0$ , which, surprisingly, is the *inverse* of the result for fluid membranes.

In this paper we present the results of a detailed study of the budding of crystalline domains in fluid membrane vesicles, using both Monte Carlo simulations and scaling arguments. The membrane is described using a network model, and the location of the budding transition is determined as a function of the spontaneous curvature of the crystalline domain,  $C_0$ , the tension of the line separating the crystalline and fluid domains,  $\lambda$ , and the radius  $R_A$  of the crystalline domain. The outline of the paper is as follows. The model and simulation technique is described in Sec. II. Simulation results for vesicle shapes, number and distribution of defects, and the budding phase diagram are presented in Sec. III, and it is shown that the budding transition occurs at a domain size  $R_A$  which is always a *decreasing* function of the the spontaneous curvature  $C_0$  for the range of parameters considered. Analytical estimates for the line budding transitions

as a function of the Young modulus, the bending rigidity, and the line tension are presented in Sec. IV. Four different scaling regimes are predicted, depending on the relative importance of the bending and stretching energies and on the domain size. A critical discussion of the analysis of Ref. [16] is also presented. Results for the dynamics of the budding transition are presented in Sec. VI. The paper closes with a brief discussion of the budding of clathrin-coated membranes.

## II. MODEL AND SIMULATION METHOD

### A. One-component membranes

For our Monte Carlo simulations of crystalline domains in fluid membranes we employ a tether-and-bead model of self-avoiding membranes [17]. The model consists of  $N$  vertices which are connected by tethers to form a triangular network. Each vertex is the center of a hard sphere of diameter  $\sigma_0 = 1$ . The tethers do not restrict the motion of connected beads for distances smaller than the tether length  $\ell_0$ , but do not allow the distance to exceed  $\ell_0$ . A Monte Carlo step then consists of  $N$  attempted positional updates with displacements chosen randomly in the cube  $[-s, s]^3$ . For tether length  $\ell_0 < \sqrt{3}\sigma_0$  and sufficiently small step sizes  $s$ , this model mimics self-avoiding membranes, since the largest allowed space between the beads is too small for other beads to penetrate the membrane. In addition, in order to allow for diffusion and fluidity within the membrane, the connectivity of the network must itself be a dynamic variable. This is usually achieved by cutting and reattaching the tethers connecting the four beads of two neighboring triangles in such a way that the two beads which were not connected before are linked by a tether after the flip. A Monte Carlo step also involves  $N$  attempted bond flips.

Tether-and-bead models have been used very successfully to study the shape and fluctuations of fluid vesicles [18,19], the passage of vesicles through narrow pores [20], and the budding dynamics of multicomponent fluid membranes [21]. In the current context, it is particularly interesting that it has been demonstrated that tether-and-bead models can be used to study the freezing transition of both planar [22] and flexible [23] membranes, as well as of flexible vesicles [24,25]. In order to induce crystallization of the membrane, no modification of the model is necessary. Instead, crystallization occurs automatically when the tether length becomes sufficiently small.

In the thermodynamic limit of very large networks, the fluid phase has been found to be stable for  $\ell_0/\sigma_0 > 1.52$  [22]. The freezing transition proceeds in two steps, from the fluid phase to a hexatic phase with quasi-long-range bond orientational but short-range translational order, and then to the crystalline phase with quasi-long-range translational order, in agreement with theoretical expectations [26]. The hexatic phase is stable within a narrow range of tether lengths,  $1.48 < \ell_0/\sigma_0 < 1.52$  [22]. For networks of finite size, the crystalline-to-hexatic and hexatic-to-fluid transitions are shifted to effectively larger tether lengths. For a network with periodic boundary conditions, the crystalline phase has been found to be stable for  $\ell_0/\sigma_0 < 1.574$  for  $N=100$ , and for  $\ell_0/\sigma_0 < 1.545$  for  $N=748$  [22].

The shape and fluctuations of fluid membranes are controlled by the curvature energy [27]

$$\mathcal{H}_b = \frac{\kappa}{2} \int dS (H - C_0)^2, \quad (1)$$

where  $\kappa$  is the bending rigidity,  $H = c_1 + c_2$  is twice the mean curvature (with principal curvature  $c_1$  and  $c_2$ ), and  $C_0$  is the spontaneous curvature. For triangulated surfaces, several discretizations of the curvature energy have been suggested [17]. Here we employ the discretization proposed by Itzykson [28], which has been shown to work very well for fluid membranes [29]. In this case, the bending energy is given by

$$\mathcal{H}_b = \frac{\kappa}{2} \sum_i \sigma_i \left[ \frac{1}{\sigma_i} \sum_{j(i)} \frac{\sigma_{ij}}{\ell_{ij}} (\mathbf{R}_i - \mathbf{R}_j) - C_0 \right]^2, \quad (2)$$

where the sum over  $j(i)$  is over neighbors of vertex  $i$ . In Eq. (2),  $\ell_{ij}$  is the distance between nodes  $i$  and  $j$  located at  $\mathbf{R}_i$  and  $\mathbf{R}_j$ , respectively,  $\sigma_{ij} = \ell_{ij} [\cot(\theta_1) + \cot(\theta_2)]/2$  is the length of a bond in the dual lattice, with angles  $\theta_1$  and  $\theta_2$  opposite to link  $ij$  in the two triangles sharing this bond, and  $\sigma_i = (1/4) \sum_{j(i)} \sigma_{ij} \ell_{ij}$  is the area of the dual cell of vertex  $i$ .

### B. Two-component membranes

The shape and fluctuations of two-component fluid membranes are again controlled by the curvature energy [27]. In addition, there is a contribution from the line tension of the domain boundary. The total energy of a two-component membrane in the strong segregation limit is given by

$$\mathcal{H} = \frac{\kappa_A}{2} \int dS (H - C_0^A)^2 + \frac{\kappa_B}{2} \int dS (H - C_0^B)^2 + \lambda \oint ds, \quad (3)$$

where  $\lambda$  is the line tension, and the bending rigidities  $\kappa_A$  and  $\kappa_B$  and spontaneous curvatures  $C_0^A$  and  $C_0^B$  are in general different for the two components. We assume for simplicity that the saddle-splay modulus  $\bar{\kappa}$  is the same for both components, so that the contribution of the Gaussian curvature is a constant and does not have to be considered.

The tether-and-bead model has been generalized to membranes with two fluid components. In this case, the two components  $A$  and  $B$  can be placed either on the surface triangles [21] or on the vertices [30,31]. In the first case, the interactions of the two-component mixture can be described by an Ising Hamiltonian, where the binary spin variables describe the occupation of the triangles with either of the two components. Since the number of neighboring triangles is always 3 in this case, the energy of the domain boundary is proportional to the number of bonds at which  $A$  and  $B$  triangles meet and is therefore independent of the membrane shape near the domain boundary, as it should be [21]. In contrast, when the Ising model with vertex occupation variables is used, the interaction energy depends on the number of neighbors. It is therefore favorable for the system to minimize the number of bonds which connect  $A$  and  $B$  vertices. Since the number of neighbors of a site is coupled to the local Gaussian curvature—with few neighbors implying a positive, and

many neighbors a negative, Gaussian curvature—the discretized curvature in combination with an Ising model with vertex variables may lead to artifacts.

However, it is not difficult to cure this problem with the vertex occupation variables. All that needs to be done is to use the *length* of the domain boundary instead of the *number* of bonds connecting  $A$  and  $B$  vertices. This is very natural in the Itzykson discretization of the curvature energy, since the variables  $\sigma_{ij}$ , which are the lengths of the bonds in the dual lattice, are already calculated anyway. The discretized version of the energy of the domain boundary is

$$\mathcal{H}_l = \lambda \sum_{\langle ij \rangle_{AB}} \sigma_{ij}, \quad (4)$$

where  $\langle ij \rangle_{AB}$  denotes the bonds connecting  $A$  and  $B$  vertices.

We want to study here crystalline domains in fluid membranes. Therefore, we have to induce crystalline order in part of the membrane by choosing an appropriately small tether length. This implies that the tether length is not uniform and depends on the type of the two connected vertices. We chose two tether lengths  $\ell_A$  and  $\ell_B$  for the  $AA$  and  $BB$  bonds, respectively, and set  $\ell_{AB} = (\ell_A + \ell_B)/2$ .

In order to complete the definition of the model, we have to specify the parameters used in the simulations. We consider a membrane with bending rigidity  $\kappa_A = \kappa_B = \kappa = 10k_B T$ . The tether length of the fluid  $B$  component is taken to be  $\ell_B/\sigma_0 = 1.68$ , safely above the fluid-to-hexatic transition at  $\ell_0/\sigma_0 = 1.52$ . The spontaneous curvature  $C_0^B$  vanishes. For the crystalline  $A$  component, we vary the parameters in the range  $0 \leq C_0^A \sigma_0 \leq 1.0$  and  $1.45 \leq \ell_A/\sigma_0 \leq 1.50$ . In the following, we use  $C_0 \equiv C_0^A$  in order to simplify the notation. Finally, line tensions in the range  $0 < \lambda \sigma_0 < 10k_B T$  are investigated. The simulations are performed for membranes of spherical topology, i.e., for vesicles, in order to avoid boundary effects and to make sure that the surface tension vanishes identically. We study three different system sizes  $(N_A, N_B) = (92, 612)$ ,  $(184, 1224)$ , and  $(368, 2442)$ , so that the total number of vertices is  $N = 704$ ,  $N = 1408$ , and  $N = 2810$ , respectively. This implies that the fraction  $x_N$  of the number of  $A$  vertices in the total number of vertices is constant, with  $x_N = 0.1307$ . For fixed tether lengths, the ratio  $x = x_N (1 + \ell_A)^2 / (1 + \ell_B)^2$  of the area of the  $A$  component to the total vesicle area is therefore also constant for the three system sizes. We have chosen a small area fraction  $x$  because we want to focus on the budding transition of an initially (almost) planar domain in a fluid membrane.

Since one of the interesting applications of our model is the budding of clathrin-coated pits, we will often denote the crystalline  $A$  domain as the “clathrin domain” in the following. This does not imply that we are taking any particular properties of clathrin molecules into account. To simplify the notation, all lengths are measured in units of the bead diameter  $\sigma_0$  and all energies in units of the thermal energy  $k_B T$ .

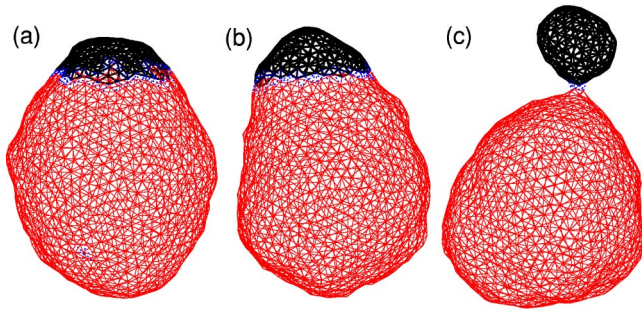


FIG. 2. (Color online) Snapshots of typical vesicle shapes for  $\ell_A = 1.50$ ,  $N_A = 184$ , and  $C_0^A = 0.1$ , with (a)  $\lambda = 1.5$ , (b)  $\lambda = 3.0$ , and (c)  $\lambda = 5.0$ . Black lines indicate bonds between  $A$  vertices.

### III. SIMULATION RESULTS: SHAPES, DEFECTS, AND THE BUDDING TRANSITION

#### A. Vesicle shapes

A sequence of typical vesicle shapes for fixed spontaneous curvature  $C_0 = 0.1$  is shown in Fig. 2. For small line tension,  $\lambda = 1.5$ , the crystalline domain takes a caplike shape. Note that the domain boundary shows strong fluctuations at this value of  $\lambda$ , which indicates the vicinity of the mixing transition of the two components. For  $\lambda = 1.5$ , the clathrin vertices remain connected during the length of a typical simulation run. For  $\lambda = 1.0$ , however, some  $A$  vertices detach from the clathrin domain and float as monomers inside the fluid membrane. Since we are interested in the strong segregation regime, we therefore restrict all simulations to values of the line tension  $\lambda \geq 1.5$ .

As the line tension increases, the crystalline domain begins to bend more strongly, while the fluctuations of the domain boundary decrease. Finally, at  $3 < \lambda < 5$ , a budding transition occurs, and the crystalline domain forms a complete bud.

This scenario is very similar to the budding transition observed in fluid membrane domains. This can be seen more clearly in a transverse projection of the vesicle shapes, which is shown in Fig. 3. The average shapes strongly resemble those calculated for phase-separated fluid membranes [32].

#### B. Defects and budding transition

In order to obtain a more detailed picture of the budding process, we have calculated several quantities that characterize the domain shape and the internal defect structure in the clathrin domain. A typical defect configuration is shown in Fig. 4.

Obviously, the length  $L$  of the boundary of the clathrin domain is well suited for characterizing the transition. The boundary length is shown in Fig. 5 as a function of the scaled line tension  $\lambda N_A^{1/2} / \kappa$ , for several values of the scaled spontaneous curvature  $C_0^A N_A^{1/2}$ . Our motivation for introducing these scaled variables is that in fluid membranes, all size dependence can be absorbed in these quantities. With increasing line tension, the curves show a rapid decrease of  $L$  for small  $\lambda$  due to the suppression of thermal fluctuations, and then a slow decay as the cap slowly curves more strongly for larger  $\lambda$ . Finally,  $L$  jumps to a very small value,

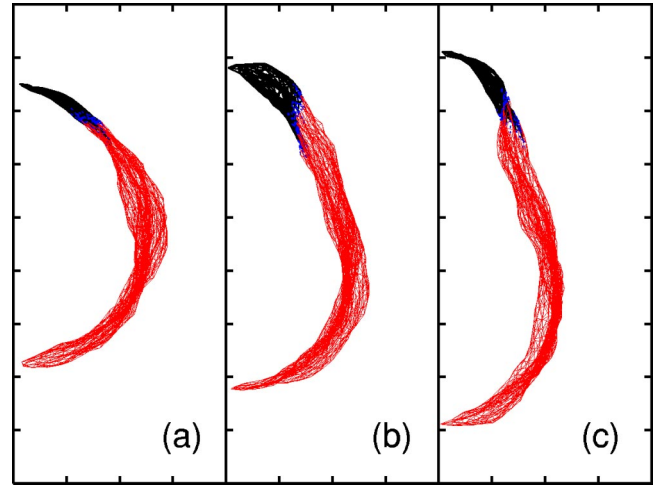


FIG. 3. (Color online) Rotationally averaged vesicle shapes for  $\ell_A = 1.50$ ,  $N_A = 184$ , with  $\lambda = 2.0$  and (a)  $C_0^A = 0.0$ , (b)  $C_0^A = 0.1$ , and (c)  $C_0^A = 0.2$ . Black lines indicate bonds between  $A$  vertices.

which indicates the first-order nature of the budding transition. This jump is large for small spontaneous curvatures and becomes smaller with increasing  $C_0$ . For  $C_0^A N_A^{1/2} \geq 4.0$ , the cap phase is not stable for our value of  $\kappa = 10k_B T$ . A comparison of the results for the scaled boundary length shown in Fig. 5 indicates that, for a given scaled spontaneous curvature  $C_0^A N_A^{1/2}$ , the transition occurs at very similar values of  $\lambda N_A^{1/2} / \kappa$  for the system sizes studied.

The bending of the initially almost flat crystalline domain is only possible when an excess of fivefold disclinations appear inside the domain. We distinguish between crystalline vertices at the boundary of the domain, which have at least one fluid vertex as a nearest neighbor, and crystalline vertices in the interior, which have only other crystalline vertices as nearest neighbors. The excess  $\Delta_{5,i}$  of fivefold coordinated vertices in the interior, i.e., the number of all fivefold coordinated vertices minus the number of all sevenfold coordinated vertices in the interior, is shown in Fig. 6. This excess is again quite small,  $\Delta_{5,i} \lesssim 3$ , in the cap phase for small  $C_0$ ,

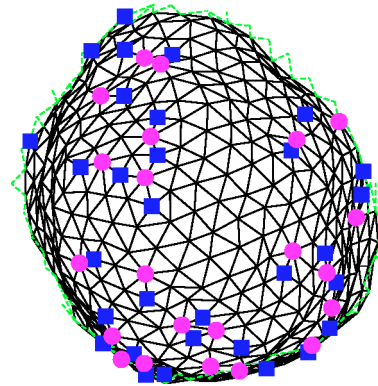


FIG. 4. (Color online) Typical defect configuration for  $N_A = 368$ ,  $\ell_A = 1.50$ ,  $\kappa = 10$ ,  $\lambda = 2.0$ , and  $C_0 = 0.1$ . The picture shows a top view of the crystalline domain; the fluid part of the membrane is not shown. fivefold and sevenfold coordinated vertices are marked by squares and circles, respectively.

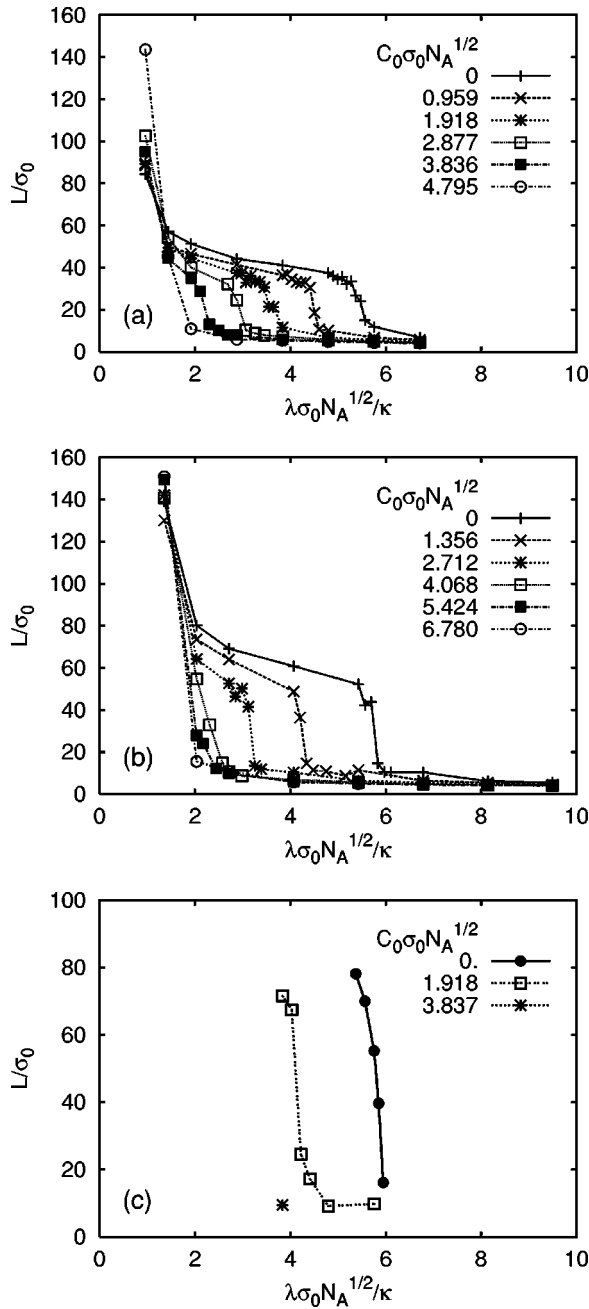


FIG. 5. The boundary length  $L$  of the clathrin domain for  $\ell_A = 1.50$  as a function of the scaled line tension  $\lambda\sqrt{N_A}/\kappa$  for three different domain sizes: (a)  $N_A=92$ , (b)  $N_A=184$ , and (c)  $N_A=368$ . In all cases, several data sets are shown for different values of the scaled spontaneous curvature  $C_0\sqrt{N_A}$ .

even very close to the budding transition, and approaches 12 in the budded phase, as required by the Euler theorem.

The deviation of  $\Delta_{5,i}$  from 12 in the latter case is due to a small number of defects in the neck region. The defect structure in this region can be characterized by the excess of fivefold coordinated vertices at the boundary. Figure 7 demonstrates that in the cap state, this number is larger for small  $\lambda$  than the excess in the interior. For larger  $\lambda$ , but before budding, the number of excess fivefold disclinations in the boundary and in the interior is almost the same. Finally, in

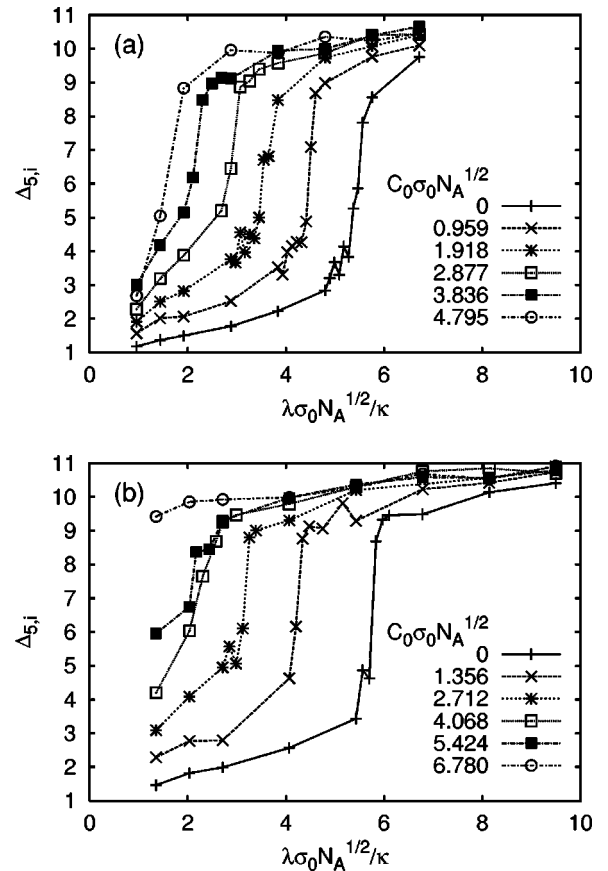


FIG. 6. Excess fivefold-coordinated vertices  $\Delta_{5,i}$  in the internal part of the clathrin domain for  $\ell_A = 1.50$  as a function of the scaled line tension  $\lambda\sqrt{N_A}/\kappa$  for two different domain sizes: (a)  $N_A=92$  and (b)  $N_A=184$ . In both cases, several data sets are shown for different values of the scaled spontaneous curvature  $C_0\sqrt{N_A}$ .

the budded state, the excess becomes *negative*, i.e., the number of sevenfold disclinations now exceeds the number of fivefold disclinations, as should be expected from a region of negative Gaussian curvature.

From these results, we can already draw the important conclusion that the fivefold disclinations are generated at the domain boundary, before they are pushed slowly into the interior of the domain by the increasing line tension. Since the density of fivefold disclinations at the boundary is higher in the cap state than in the interior, the boundary must also curve more strongly, while the interior remains flatter.

In Fig. 8, we show the number  $n_5^{(iso)}$  of isolated fivefold disclinations, i.e., of fivefold coordinated vertices, that have only sixfold coordinated nearest neighbors. With  $n_5^{(iso)} \leq 1$  for small  $C_0$ , this number is quite small in the cap phase and jumps to about  $n_5^{(iso)} \approx 6$  in the budded phase. Since the Euler theorem requires an excess of 12 fivefold disclinations, we conclude that only half of these disclinations are isolated, while the other half are dressed by neighboring dislocations. Figure 8 indicates that for larger system sizes the number of dressed fivefold disclinations increases.

Other quantities that characterize the internal order of the crystalline phase are the total number of defects—defined as the total number of five- and sevenfold coordinated

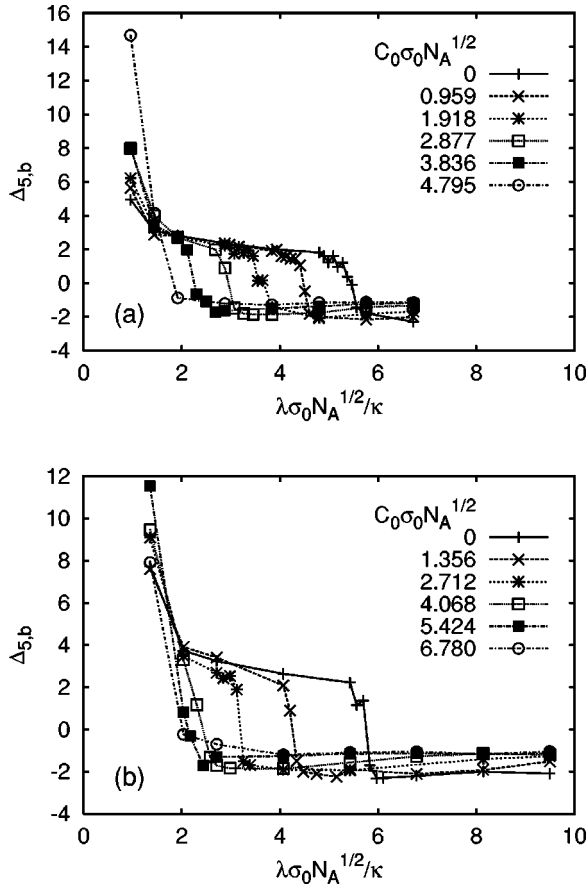


FIG. 7. Excess of fivefold coordinated vertices,  $\Delta_{5,b}$ , at the boundary of the clathrin domain for  $\ell_A = 1.50$  as a function of the scaled line tension  $\lambda\sqrt{N_A}/\kappa$  for two different domain sizes: (a)  $N_A = 92$  and (b)  $N_A = 184$ . In both cases, several data sets are shown for different values of the scaled spontaneous curvature  $C_0\sqrt{N_A}$ .

vertices—in the interior,  $\Sigma_i$ , and at the boundary,  $\Sigma_b$ , of the clathrin domain (see Figs. 9 and 10). At the budding transition, the jump in the total number of defects in the interior is quite pronounced. In the cap phase, near the budding transition, the total number of defects minus the number of topological disclinations,  $\Sigma_i - \Delta_{5,i}$ , increases roughly as the domain area (compare Figs. 9 and 6). On the other hand, in the budded phase,  $\Sigma_i - \Delta_{5,i}$  increases more rapidly, from about 8 for  $N_A = 92$  to about 20 for  $N_A = 184$ . Figure 10 demonstrates that the total number of defects at the boundary is roughly proportional to the boundary length (see Fig. 5).

The location of the budding transition can be determined from these simulation data. The dependence of the scaled spontaneous curvature  $C_0\sqrt{N_A}$  on the scaled line tension  $\lambda\sqrt{N_A}/\kappa$  at the budding transition is shown in Fig. 11. The transition points were determined from the point of intersection of a horizontal line of constant boundary length  $L^*$  with the interpolated data plotted in Fig. 5.  $L^*$  has been chosen to lie approximately halfway between the two values of the domain lengths at the cap-to-bud transition ( $L^* = 20$  for  $N_A = 92$ ,  $L^* = 30$  for  $N_A = 184$ , and  $L^* = 40$  for  $N_A = 368$ ).

For all three system sizes, the data are consistent with

$$\lambda R_A / \kappa + \gamma C_0^A R_A = \Gamma(R_A) \quad (5)$$

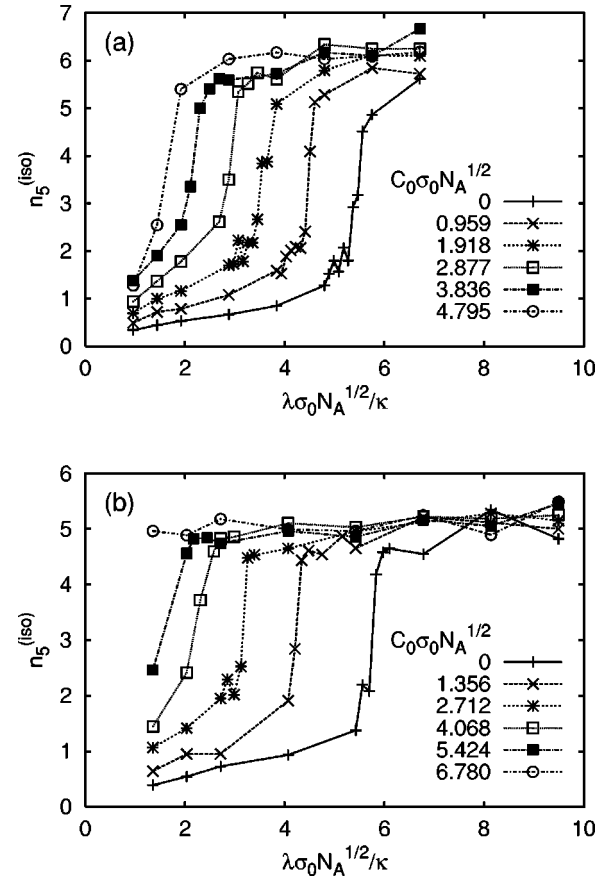


FIG. 8. The number of isolated fivefold disclinations,  $n_5^{(iso)}$ , in the clathrin domain for  $\ell_A = 1.50$  as a function of the scaled line tension  $\lambda\sqrt{N_A}/\kappa$  for two different domain sizes: (a)  $N_A = 92$  and (b)  $N_A = 184$ . In both cases, several data sets are shown for different values of the scaled spontaneous curvature  $C_0\sqrt{N_A}$ .

at the transition, where  $R_A$  is the radius of the planar, circular clathrin domain, with  $\pi R_A^2 = 2N_A\sqrt{3}\langle\ell\rangle/4$  to leading order, and average bond length  $\langle\ell\rangle \approx (1 + \ell_A)/2$  of AA bonds. We have determined  $R_A$  numerically from the area of the clathrin domain. The resulting values of  $R_A$  exhibit a weak dependence on the spontaneous curvature and the line tension. At the budding transition,  $R_A$  is found to be about 10% smaller in the cap phase than in the budded phase. In the following, we have used the latter value.

In Eq. (5), the prefactor of the first term is normalized to unity. The prefactor  $\gamma$  of the second term is found to be close to unity for the two smaller system sizes studied, with  $\gamma = 0.84$ , while the function  $\Gamma(R_A)$  has the values

$$\Gamma(R_A) = \begin{cases} 3.39 \pm 0.02 & \text{for } N_A = 92, R_A = 6.18, \\ 3.45 \pm 0.03 & \text{for } N_A = 184, R_A = 8.74, \\ 3.68 \pm 0.05 & \text{for } N_A = 368, R_A = 12.4. \end{cases} \quad (6)$$

We can therefore draw the conclusion that  $\Gamma(R_A)$  has only a weak system size dependence.

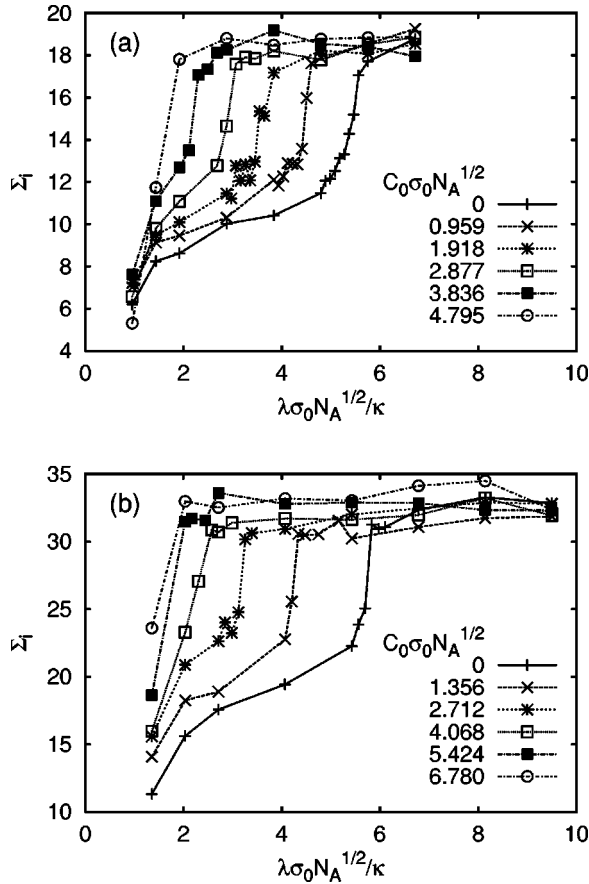


FIG. 9. Total number of defects,  $\Sigma_i$ , in the internal area of the clathrin domain for  $\ell_A = 1.50$  as a function of the scaled line tension  $\lambda\sqrt{N_A}/\kappa$  for two different domain sizes: (a)  $N_A = 92$  and (b)  $N_A = 184$ . In both cases, several data sets are shown for different values of the scaled spontaneous curvature  $C_0\sqrt{N_A}$ .

### C. Dependence on the Young modulus

All the data we have presented so far have been calculated for fixed tether length  $\ell_A = 1.50$ . For the system sizes studied in the simulation, this tether length is well in the crystalline phase; however, in the thermodynamic limit, this tether length is in the center of the hexatic phase. We have therefore also investigated the behavior for a smaller tether length,  $\ell_A = 1.45$ , which is well within the crystalline phase even in the thermodynamic limit. The comparison of the data for the two tether lengths allows an estimate of the effect of the size of the Young modulus, which characterizes the in-plane elasticity, on the defect distributions and on the phase behavior.

Two characteristic quantities, the boundary length  $L$  and the number  $\Delta_{5,i}$  of excess fivefold disclinations in the interior area are shown in Figs. 12 and 13, respectively. This shows two qualitative effects with decreasing tether length (i.e., increasing Young modulus): (i) the budding transition is shifted to slightly higher values of the scaled line tension, and (ii) there are fewer excess defects in the cap phase and more excess defects in the budded phase. A more quantitative analysis of the Monte Carlo data will be made in Sec. IV below.

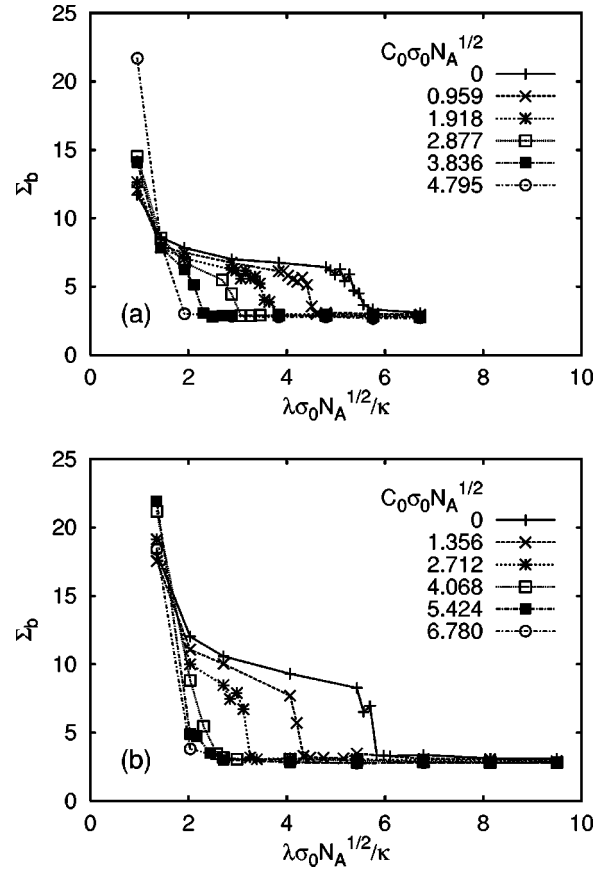


FIG. 10. Total number of defects,  $\Sigma_b$ , at the boundary of the clathrin domain for  $\ell_A = 1.50$  as a function of the scaled line tension  $\lambda\sqrt{N_A}/\kappa$  for two different domain sizes: (a)  $N_A = 92$  and (b)  $N_A = 184$ . In both cases, several data sets are shown for different values of the scaled spontaneous curvature  $C_0\sqrt{N_A}$ .

### IV. ANALYTICAL ESTIMATES OF THE LINE OF BUDDING TRANSITIONS

The location of the budding transition can be calculated analytically for some special cases. A comparison of these

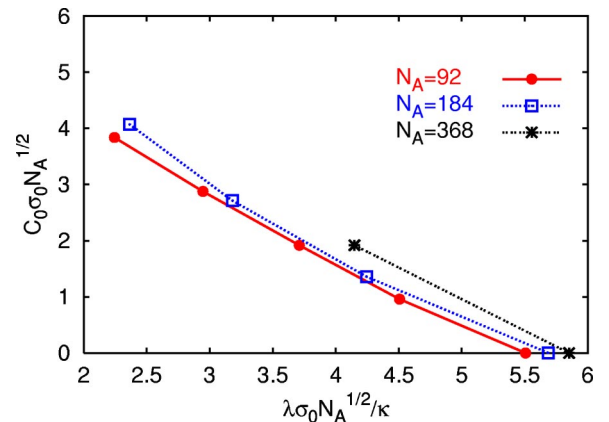


FIG. 11. (Color online) Dependence of the scaled spontaneous curvature  $C_0\sqrt{N_A}$  on the scaled line tension  $\lambda\sqrt{N_A}/\kappa$  at the budding transition, for  $\ell_A = 1.50$  for three different domain sizes:  $N_A = 92$ ,  $N_A = 184$ , and  $N_A = 368$ .

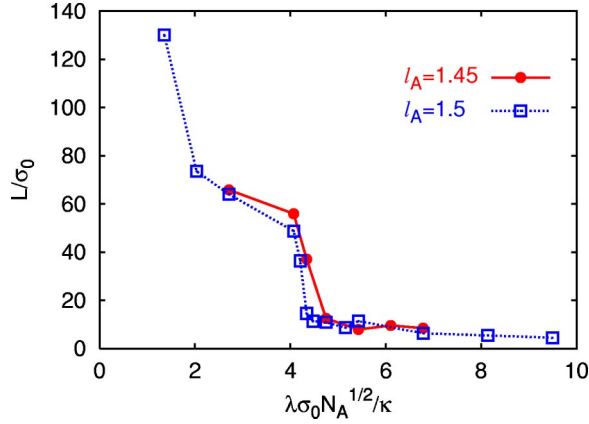


FIG. 12. (Color online) The boundary length  $L$  of the clathrin domain for  $\ell_A = 1.50$  and  $\ell_A = 1.45$  as a function of the scaled line tension  $\lambda\sqrt{N_A}/\kappa$  for domain size  $N_A = 184$  and scaled spontaneous curvature  $C_0\sqrt{N_A} = 1.356$ .

estimates with our numerical data will lead to a consistent picture of the budding of crystalline domains in vesicles.

### A. Fluid domains of spherical shape

Jülicher and Lipowsky [32,33] have calculated the locus of budding transitions for axisymmetric vesicles consisting of one fluid domain with spontaneous curvature  $C_0^A$  embedded in a fluid membrane of spontaneous curvature  $C_0^B$ . They solve the shape equations numerically and thereby determine the line of budding transitions. They also derive an analytical estimate for this line by approximating the incomplete bud by a spherical cap and the complete bud by two spheres. For the case of  $C_0^B = 0$  and  $\kappa_A = \kappa_B$  considered here, this estimate is given by

$$\frac{\lambda}{\kappa} R_0 = \frac{2}{\sqrt{x(1-x)}} [1 + C_0^A R_0 (x - \sqrt{x})], \quad (7)$$

where  $R_0$  is the radius of a spherical vesicle of the same area. Equation (7) was found to be a lower bound for the transition

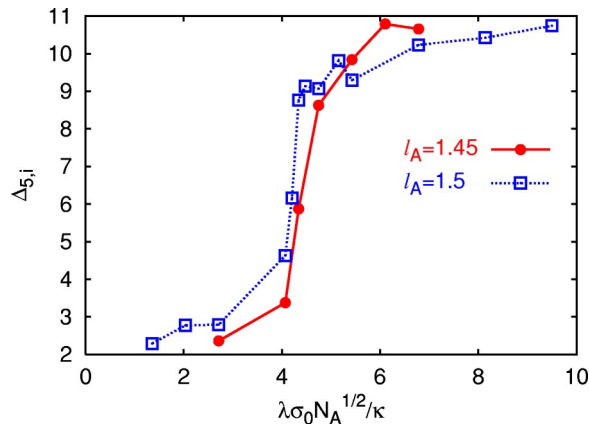


FIG. 13. (Color online) The number of excess fivefold disclinations in the interior of the clathrin domain for  $\ell_A = 1.50$  and  $\ell_A = 1.45$  as a function of the scaled line tension  $\lambda\sqrt{N_A}/\kappa$  for domain size  $N_A = 184$  and scaled spontaneous curvature  $C_0\sqrt{N_A} = 1.356$ .

and to approximate the numerically determined line of budding transitions quite accurately. This estimate can easily be adapted to our case. With  $R_0 = R_A / (2\sqrt{x})$ , we obtain

$$\frac{\lambda}{\kappa} R_A + \frac{1 - \sqrt{x}}{\sqrt{1-x}} C_0^A R_A = 4 \frac{1}{\sqrt{1-x}}. \quad (8)$$

For  $x_N = 0.13$ , which corresponds to  $x = 0.104$  for  $\ell_A = 1.50$ , this implies

$$\frac{\lambda}{\kappa} R_A + 0.716 C_0^A R_A = 4.225. \quad (9)$$

Another estimate can be obtained by considering the limit shape of budded vesicles. The limit shape corresponds to an infinitesimal neck, for which Jülicher and Lipowsky [32] derived the condition

$$\frac{\lambda}{\kappa} R_A + C_0^A R_A = 4 + 4\sqrt{x/(1-x)} = 5.363 \quad (10)$$

for  $x = 0.104$ . This condition must obviously be an upper bound for the location of the budding transition.

### B. The argument of Mashl and Bruinsma for crystalline domains

In order to calculate the location of the budding transition of a crystalline domain, Mashl and Bruinsma [16] considered a membrane domain of radius  $R_A$  with a fivefold disclination at the center and a sevenfold disclination at distance  $r$ . In this scenario, the budding transition is determined by the location of the unbinding of this dislocation pair. They approximate the bending energy of this *buckled* configuration by

$$E_b = 2\kappa C_0^A R_A \Lambda(r/R_A) + \frac{\pi}{2} \kappa (C_0^A R_A)^2, \quad (11)$$

where  $\Lambda(0) = 0$  and  $\Lambda(1) = -\pi/\sqrt{3}$ . For intermediate values of  $r/R_A$ ,  $\Lambda$  has to be calculated numerically. The contribution of the stretching energy was estimated to be the energy of a dislocation of Burgers vector  $r$  in a *buckled* crystalline membrane with  $C_0 = 0$ ,

$$E_s = K_0 r^2 \left[ \frac{1}{8\pi} \ln(R_b/\langle \ell \rangle) + c(\bar{\kappa}/\kappa) \right], \quad (12)$$

which was calculated in the limit of *infinite* membrane size by Seung and Nelson [34]. In Eq. (12),  $R_b$  is the buckling radius of a dislocation, and  $c(\bar{\kappa}/\kappa)$  depends only on the ratio of the bending rigidity  $\kappa$  and the saddle-splay modulus  $\bar{\kappa}$ . Using the sum of Eqs. (11) and (12) as an ansatz for the free energy, Mashl and Bruinsma [16] found that the minimum of this energy moves continuously from  $r = 0$  to larger values of  $r$  with increasing  $C_0$ , reaching  $r = R_A$  at some value of  $\kappa C_0^A / (K_0 R_A)$ , which signals the budding transition. This results implies, in particular, that  $C_0^A \sim R_A$  at the transition.

We believe that this estimate of the free energy of a buckled disclination pair is incorrect. This can be seen easily by

considering the case  $r=R_A$ . In this case, the sevenfold disclination no longer contributes, and we have a cone with a fivefold disclination at the center. In the inextensional limit of large  $K_0$ , the total energy can be calculated exactly and is found to be

$$E_{cone} = \pi\kappa \left[ \frac{11}{30} \ln(R_A/\langle\ell\rangle) - 2\frac{\sqrt{11}}{\sqrt{30}} C_0^A R_A + \frac{1}{2} (C_0^A R_A)^2 \right] + \frac{\pi}{3} \bar{\kappa} + E_{core} \quad (13)$$

which essentially agrees with Eq. (11), up to an additive contribution with a logarithmic size dependence. In this case, the stretching energy vanishes, so that Eq. (12) strongly overestimates the stretching contribution. The origin of this disagreement is the fact that Eq. (12) is valid only in the limit  $r \ll R_A$  [34].

### C. Crystalline sphere with disclinations and grain boundaries

Bowick, Nelson, and Travesset [35] have recently calculated the energy of an icosahedral lattice on a perfect spherical surface which contains no defects other than the topologically required 12 disclinations. For a sphere of radius  $R_0$ , the elastic energy was found to be

$$E_{ico} = C_{ico} \frac{\pi K_0}{36} R_0^2 + 12E_{core} \quad (14)$$

with  $C_{ico}=0.604$ , where  $K_0$  is the two-dimensional Young modulus. For a vesicle with large bending rigidity, i.e., with  $\kappa \gg K_0 \langle\ell\rangle^2$ , where  $\langle\ell\rangle = (1 + \ell_A)/2$  is the average bond length in the clathrin domain, we can use this result to estimate the position of the budding transition by comparing this energy with that of a planar patch of the same area, i.e., with  $R_A = 2R_0$ . For the sphere, the energy is a sum of the stretching energy (14) and the curvature energy (1). The energies of the planar and budded configurations are equal when

$$\frac{\lambda}{\kappa} R_A + 2C_0 R_A = 4 + \frac{C_{ico}}{288} \frac{K_0 R_A^2}{\kappa} + 12 \frac{E_{core}}{2\pi\kappa}. \quad (15)$$

In order to see whether the stretching term contributes, we have to insert values for  $K_0$  and  $R_A$  that are characteristic for our simulation. In Ref. [25], it was shown that the two-dimensional Young modulus  $K_0$  for planar, crystalline networks of the type employed in our simulations increases with decreasing tether length  $\ell_0$ . In particular, the values  $K_0 \langle\ell\rangle^2 = 64.8$  for  $\ell_A = 1.50$  and  $K_0 \langle\ell\rangle^2 = 78.0$  for  $\ell_A = 1.45$  were obtained [25]. For  $R_A = 12.5$ , the largest domain size considered in the simulations, this implies  $(C_{ico}/288)K_0 R_A^2/\kappa \approx 1.36$  for  $\ell_A = 1.50$  and  $(C_{ico}/288)K_0 R_A^2/\kappa \approx 1.70$  for  $\ell_A = 1.45$ . For a crystalline sphere, stretching contributions are therefore subdominant on the right-hand side of Eq. (15) for the range of domain sizes investigated.

Bowick, Nelson, and Travesset [35] have shown that short grain boundaries at the location of the topological disclina-

tions screen the strain field and lead to a reduction of the energy of a crystalline lattice on a sphere. For grain boundaries containing  $n$  dislocations per disclination,  $C_{ico}(n)$  decreases from 0.60, 0.44, 0.37 for  $n=0,1,2$ , respectively, to  $C_{ico}(n) \approx 0.25$  for large  $n$  [35]. The effect of the stretching contribution in Eq. (15) is therefore reduced by grain boundaries. Indeed, in the configurations shown in Fig. 15 below, several grain-boundary lines are visible. The data for the total number of defects in the interior of the crystalline domain shown in Fig. 9 indicate that there is about 0.5 dislocation per topological fivefold disclination for  $N_A = 92$ , and about 1.5 for  $N_A = 184$ .

### D. Crystalline icosahedron without defects

When the two-dimensional Young modulus is sufficiently large, bending is more favorable than stretching, and the curvature is no longer distributed uniformly over the bud [36]. Instead, the stress becomes localized in ‘‘stretching ridges’’ which connect the 12 fivefold disclinations. The bud then takes the shape of an icosahedron with rounded edges and nearly flat faces. For large system sizes, and no defects beyond the topologically required fivefold disclinations, the energy of such a shape was shown from elasticity theory and simulations to be [36–38]

$$E_{teth} = \frac{11}{5} \pi\kappa \ln\left(\frac{N_A}{12}\right) + C_{teth} \kappa \left(\frac{K_0}{\kappa}\right)^{1/6} R_A^{1/3} + 12E_{core}, \quad (16)$$

where the first term is the contribution of the cone-shaped corners and the second of the ridges. The prefactor  $C_{teth}$  can be extracted from simulations of tethered networks [37,38], and has been found to be  $C_{teth} = 3.63$  for icosahedra [38] and  $C_{teth} = 9.3$  for tetrahedra [37].

It is interesting to note that the simulations of Refs. [37,38] show that for  $C_0=0$  the contribution of the cone-shaped corners dominates up to quite large system sizes. Only for  $(K_0/\kappa)^{1/2} R_A$  in the range of 500 to 1500 do the ridges begin to dominate the curvature energy. This can easily be seen from Eq. (16), where the contributions of corners and ridges are equal when

$$\left(\frac{K_0}{\kappa}\right)^{1/2} R_A = \left[ \frac{11\pi}{5C_{teth}} \ln[N_A/12] \right]^3. \quad (17)$$

We now compare the free energies of a planar disk and a deformed sphere, which we consider to be composed of 12 cones. The membrane area of a cone corresponding to a fivefold disclination is  $(6/5)\pi R_0^2$ . This implies  $R_A^2 = (72/5)R_0^2$  and

$$\frac{\lambda}{\kappa} R_A + 2 \sqrt{\frac{11}{10}} C_0^A R_A = 12 \frac{E_{teth}}{2\pi\kappa} \quad (18)$$

so that  $\Gamma(R_A)$  exhibits a logarithmic dependence when the energy contribution of the cone-shaped corners dominates. For large values of  $(K_0/\kappa)^{1/2} R_A$ ,  $\Gamma(R_A)$  is proportional to  $R_A^{1/3}$ .

### E. Hexatic domains of cone-shape

In crystalline membranes that are larger than the buckling radius  $R_b$  of a dislocation, the elastic (curvature and stretching) energy of a free dislocation has been predicted to approach a constant, independent of system size [34]. This prediction has been confirmed by Monte Carlo simulations [24,25] of the same network model that is employed in the current study. Therefore, the free energy of dislocations is negative for any finite temperature for a sufficiently large membrane. This implies that a finite concentration of free dislocations is present in the membrane, which destroys translational order. The resulting phase, which still has bond-orientational order, is called a hexatic.

The energy  $E_5$  of a cone-shaped membrane in the hexatic phase was calculated in Refs. [39,40], with the result

$$\frac{E_5}{\pi K_H} = \left\{ 2 \left[ \left( \frac{25}{36} + \frac{\kappa}{K_H} \right) \left( 1 - \frac{\kappa}{K_H} \right) \right]^{1/2} - \frac{5}{3} \right\} \ln(R_0 / \langle \ell \rangle) \quad (19)$$

for  $\kappa/K_H < 11/72$  and

$$\frac{E_5}{\pi K_H} = \frac{1}{36} \ln(R_0 / \langle \ell \rangle) \quad (20)$$

for  $\kappa/K_H > 11/72$ , where  $K_H$  is the hexatic stiffness and  $R_0$  is the radius of the base area of the cone. The budding transition is again described by Eq. (18), with  $E_{teth}$  replaced by  $E_5$ . This result implies that  $\Gamma(R_A)$  exhibits a logarithmic dependence for sufficiently large  $R_A$ .

In order to proceed, we need an estimate of the magnitude of the ratio  $\kappa/K_H$ . Such an estimate can be obtained by comparing the calculated phase diagram as a function of  $\kappa$  and  $K_H$  [41] with the phase diagram obtained from Monte Carlo simulations of our model [24,25]. Since  $K_H$  is not known in the simulations, the phase diagram was plotted as a function of the Young modulus  $K_0$  of a membrane with the same tether length, but without any defects. The two phase diagrams have very similar shapes. Therefore, we assume  $K_H = \alpha K_0 \langle \ell \rangle^2$ , with a proportionality constant  $\alpha$  which is obtained from fitting the location of the hexatic-to-fluid transition, which occurs at  $k_B T / K_H = \pi/72 = 0.0436$  [41] and at  $k_B T / (K_0 \langle \ell \rangle^2) = 0.0172$  [21]. This implies  $\alpha = 0.4$ . From the simulation results for  $K_0 \langle \ell \rangle^2$  [25], we then find  $K_H = 25.8$  for  $\ell_A = 1.50$  and  $K_H = 31.2$  for  $\ell_A = 1.45$ . Thus, for  $\kappa = 10$ , we obtain  $\kappa/K_H \approx 0.39 > 11/72$  and  $\kappa/K_H \approx 0.32 > 11/72$  for  $\ell_A = 1.50$  and  $\ell_A = 1.45$ , respectively. Therefore, for our range of simulated tether lengths,  $12E_5 / (2\pi\kappa) = [K_H / (6\kappa)] \ln(R_0 / \langle \ell \rangle)$ . This yields a logarithmic dependence with a prefactor of  $K_H / (6\kappa) \approx 0.5$ .

It is interesting to note that renormalization group calculations for fluctuating planar membranes predict that the ratio  $K_H / \kappa$  approaches the universal value  $K_H / \kappa = 4$  in the long-wavelength limit in the hexatic, “crinkled” phase [41,42]. Our estimate of  $K_H / \kappa \approx 3$  in the short-wavelength regime indicates that corrections to scaling can be expected to be small.

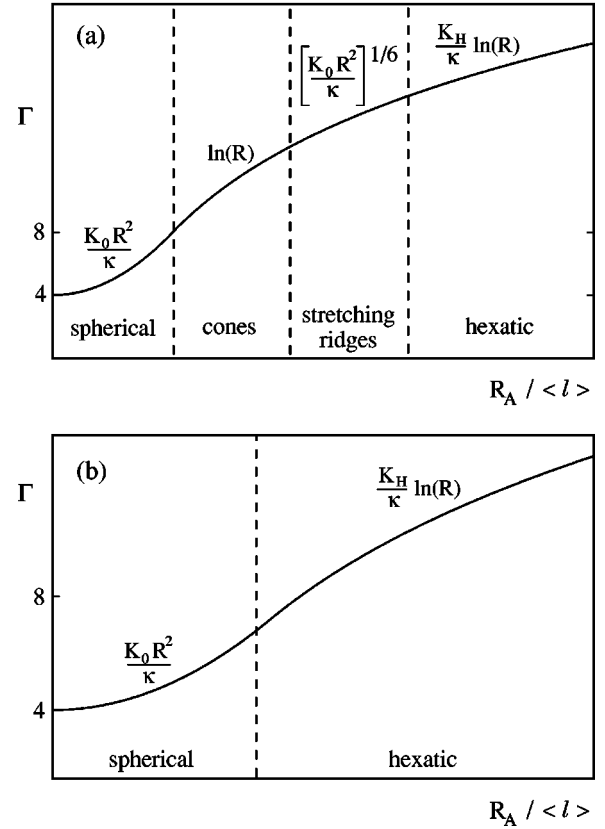


FIG. 14. Scaling regimes for the function  $\Gamma$ , which characterizes the dependence of the budding transition on the radius  $R_A$  (in units of the average bond length  $\langle \ell \rangle$ ) of a planar crystalline domain. (a) Low defect density and high Young modulus. (b) High defect density and low Young modulus. “Spherical” denotes the regime of spherical bud shapes, “cones” the regime where the fivefold dislocations are cone shaped, “stretching ridges” the regime where the competition of bending and stretching leads to stress condensation along the edges of an icosahedron, and “hexatic” the regime where free dislocations induce hexatic order in the membrane. In the spherical regime, short grain boundaries reduce the stretching energy.

### V. DISCUSSION OF BUDDING SCENARIOS

From the various theoretical results described in the previous subsections, together with the simulation data, the following picture emerges. The budding behavior depends on the value of the ratio  $Q = K_0 R_A^2 / \kappa$ , on the buckling radius  $R_b / \langle \ell \rangle \sim \kappa / (K_0 \langle \ell \rangle^2)$  of a dislocation, measured in units of the average nearest-neighbor distance, and on the distance from the two-dimensional melting transition, which is determined by the value of  $K_0 \langle \ell \rangle^2$ . There are various scenarios, depending on the values of the buckling radius and  $K_0 \langle \ell \rangle^2$ .

Two possible scenarios are sketched in Fig. 14. Consider first the case of large buckling radius and very low defect density, [See Fig. 14(a)]. Then, for small domain sizes  $R_A$ ,  $Q$  is small, the bud is spherical, and the membrane is crystalline without excess defects. This is the case discussed in Sec. IV C. With increasing size, defect scars in the form of short grain boundaries appear at the location of the 12 fivefold disclinations. The spherical shape begins to deform into

an icosahedral shape with stretching ridges connecting the 12 topological disclinations (compare Sec. IV D). Finally, the system size becomes so large that the free energy of a free buckled dislocation,

$$F_{disloc} = \frac{1}{8\pi} K_0 \langle \ell \rangle^2 \ln(R_b / \langle \ell \rangle) - k_B T \ln(\pi R_A^2 / \langle \ell \rangle^2), \quad (21)$$

becomes negative and the membrane enters the hexatic phase discussed in Sec. IV E. This happens when

$$\pi(R_A / \langle \ell \rangle)^2 = (R_b / \langle \ell \rangle)^{(1/8\pi)(K_0 \langle \ell \rangle^2 / k_B T)}, \quad (22)$$

where the exponent on the right-hand side is close to 2 in the vicinity of the crystal-to-hexatic transition for the planar system, but becomes very large at small tether lengths.

The crossover from the regime of a spherical crystal with defect scars to the regime of a rounded icosahedron without defects can be estimated by equating the energies of Eqs. (14) and (16). This corresponds to

$$Q = \frac{1584}{5C_{ico}} \ln\left(\frac{N_A}{12}\right), \quad (23)$$

where we have assumed that the system is small enough that for the icosahedron the energy is dominated by the contribution from the corners. For crystalline domains with smaller values of  $Q$ , the shape should be spherical with defect scars; for domains with larger  $Q$  rounded icosahedrons should be observed. For  $N=500$ , this implies  $Q=2410$ . At the crossover point, the contribution of the stretching energy in Eq. (15) roughly equals the contribution of the bending energy.

The crossover from the crystalline to the hexatic phase is determined by the ratio  $R_A/R_b$  of the buckling radius  $R_b$  and the domain size. For *open* membranes with free boundary conditions, the buckling radius has been calculated in Ref. [34] to be  $R_b = \Xi(\bar{\kappa}/\kappa)\kappa/(K_0\langle\ell\rangle)$ . The scaling function  $\Xi(\bar{\kappa}/\kappa)$  depends on the ratio of the saddle-splay modulus  $\bar{\kappa}$  and the bending rigidity  $\kappa$ . The Gaussian-curvature term in the curvature Hamiltonian has to be taken into account for open membranes, since it determines the boundary conditions. For  $\bar{\kappa}/\kappa=0$ , where the curvature Hamiltonian becomes unstable with respect to the formation of saddle-shaped structures with small radii of curvature, the buckling radius vanishes. Similarly, the buckling radius vanishes for  $\bar{\kappa}/\kappa=-2$ , where the curvature Hamiltonian has an instability toward the formation of small vesicles. In the range  $-2 < \bar{\kappa}/\kappa$ , fluid membranes with large radii of curvature are stable, and the buckling radius is finite, with a maximum at  $\bar{\kappa}/\kappa \approx -0.8$  where  $\Xi \approx 125$ .

For *vesicles* or membranes with periodic boundary conditions which are characterized by a uniform saddle-splay modulus, the Gauss-Bonnet theorem indicates that the integral over the Gaussian curvature is a topological invariant which does not affect the membrane shape and fluctuations. Therefore, the buckling radius cannot depend on  $\bar{\kappa}$  in this case. However, periodic boundary conditions or the spherical topology of a vesicle can be expected to have a similar constraining effect on buckling as the most unfavorable value of

$\bar{\kappa}$  for open boundaries. We therefore propose that, for vesicles, the value of the buckling radius for open membranes with  $\bar{\kappa} = -\kappa$  should be used. For  $\ell_0 = 1.50$  and  $\kappa = 10$ , this implies  $R_b = 25$ .

Consider now a system with a small buckling radius and a high defect density [see Fig. 14(b)]. In this case, for small domain sizes, we again expect spherical shapes with short grain boundaries. However, for larger sizes there should be a direct crossover to hexatic membranes.

The main conclusion that can be drawn from the preceding analysis is that, in general, we predict a *weak size dependence* of  $\Gamma(R_A)$  in Eq. (5), with several distinct scaling regimes [43]. In particular, the value of the line tension or the spontaneous curvature at the budding transition is a decreasing function of  $R_A$ . This result is strongly supported by our simulation data. In our simulations,  $Q=415$  for  $\ell_A=1.50$  and  $R_A=10$ . The parameters in the simulations are therefore such that we are in the crossover regime from the crystalline to the hexatic phase: defect scars can be recognized, the buckling radius is on the order of the domain size, the stretching energy is comparable to the bending energy, and small deviations from the spherical shape are visible.

We can make the comparison of the Monte Carlo data and the analytical estimates more *quantitative* by studying the dependence of the budding transition on the domain size. First, for the Monte Carlo data, the prefactor  $\gamma$  of the spontaneous curvature term in Eq. (5) is found to be  $\gamma=0.84$ , slightly smaller than, but close to unity, in good agreement with the predictions for fluid vesicles [compare Eqs. (9) and (10)]. On the other hand, the prefactor of the spontaneous curvature term in all our estimates for crystalline and hexatic membranes was found to be  $\gamma=2$ . However, this can easily be traced back to the fact that in the latter cases we do not take into account that the cap has a curved shape. Rather, we simply compare the free energies of *flat* domains and spherical buds. The same approximation would also lead to  $\gamma=2$  for fluid domains. We therefore believe that our analytical results for crystalline and hexatic domains overestimate this prefactor.

Second, we have seen in Figs. 5–10 that the budding transition disappears for  $C_0\sigma_0N_A^{1/2} \approx 4$ , which corresponds to  $C_0R_A \approx 2.6$ . This result can easily be understood on the basis of Eq. (5). For this value of  $C_0R_A$ , the two sides of Eq. (5) become equal for a line tension  $\lambda\sigma_0$  on the order of  $k_B T$ . The line tension is so small in this case that we are very close to the mixing critical point of the two components.

Third, we can compare the dependence of  $\Gamma(R_A)$  obtained from the Monte Carlo data with the prediction (15) for crystalline buds with grain boundaries. The numerical data for  $\ell_A=1.50$  are well described by  $\Gamma(R_A) = 3.28 + 0.0004K_0R_A^2/\kappa$ . The numerical prefactor of the second term should be compared with  $C_{ico}(n)/288$ , which is 0.001 for  $n=2$ . Since we have additional dislocations in the simulated domains due to the vicinity of the hexatic phase, these two results are in very nice agreement.

An important point we have not discussed yet is the dependence of  $\Gamma(R_A)$  on the two-dimensional Young modulus  $K_0$ . In the defect-free crystalline phase, Eq. (14) implies a

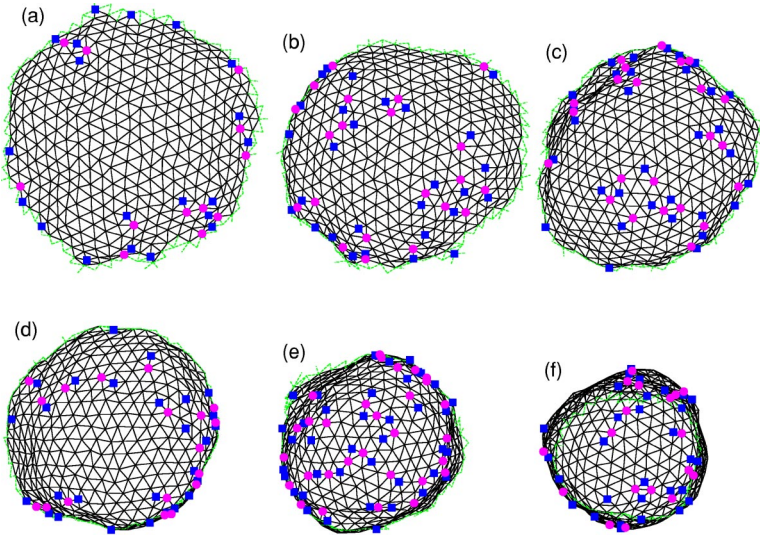


FIG. 15. (Color online) Snapshots of configurations during the budding process after a quench from a completely spherical initial state. The pictures show a top view of the crystalline domain; the fluid part of the membrane is not shown. Fivefold and sevenfold coordinated vertices are marked by squares and circles, respectively. The parameters are  $N_A=368$ ,  $\ell_A=1.50$ ,  $\lambda=2.0$ , and  $C_0^A=0.2$ . Snapshots are shown at time (a)  $t=0.1 \times 10^6$ , (b)  $t=0.3 \times 10^6$ , (c)  $t=0.5 \times 10^6$ , (d)  $t=1 \times 10^6$ , (e)  $t=2 \times 10^6$ , and (f)  $t=3 \times 10^6$  Monte Carlo steps after the quench.

linear dependence on  $K_0$ . With the numbers appropriate for our simulations, a change of the tether length from  $\ell_A=1.50$  to  $\ell_A=1.45$  implies a shift  $\Delta\Gamma(R_A)=0.21$ . This result is consistent with the small shift observed in the simulations, (see Figs. 12 and 13).

It is worth mentioning that we would obtain a quadratic  $R_A$  contribution to  $\Gamma$  in the regime of crystalline buds which is reminiscent of the result of Mashl and Bruinsma [16] if the contribution of the stretching energy in Eq. (15) were larger than that of the bending energy. However, it is important to note that (i) the physical origin of this contribution is different, since in our case, it arises from the stretching of a crystalline cone when it is deformed into a spherical cap, while it comes from the energy of a disclination pair in theirs, and (ii) the stretching contribution, which is proportional to  $K_0 R_A^2$ , can never dominate the bending energy, since the bud begins to deform into an icosahedral shape before this can happen.

## VI. DYNAMICS OF THE BUDDING TRANSITION

### A. Formation of single buds

In Sec. III we studied the shapes, defect distributions, and phase behavior of two-component vesicles in thermal equilibrium.

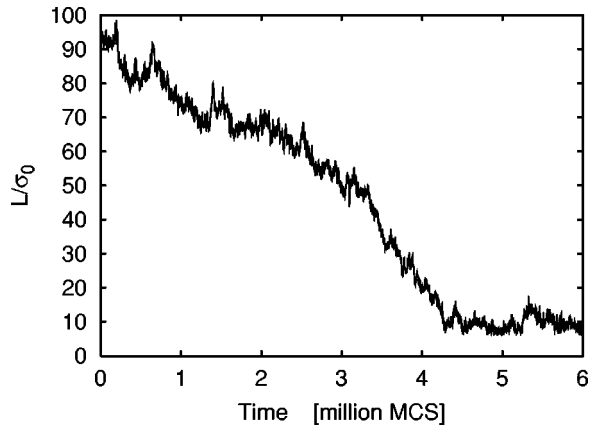


FIG. 16. Time dependence of the boundary length  $L$  of the clathrin domain for  $N_A=368$ ,  $\ell_A=1.50$ ,  $\lambda=2.0$ , and  $C_0^A=0.2$ . See Fig. 15 for the corresponding configurations.

Another interesting question is the dynamical behavior after the system has been quenched from a state of vanishing spontaneous curvature,  $C_0^A=0$ , to a part of the phase diagram where single buds are stable. Here, the question arises as to how the defects appear dynamically in the clathrin domain.

Several snapshots of configurations during the budding process are shown in Fig. 15 for a system with  $C_0^A=0.2$  after the quench. The figure demonstrates very nicely that fivefold and sevenfold disclinations are generated at the domain boundary, and that the fivefold disclinations then move into the internal area of the clathrin patch.

The time dependence of the boundary length and the excess number of fivefold disclinations in the interior of the clathrin domain are shown in Fig. 16 and Fig. 17, respectively. From these figures, the following time regimes can be distinguished.

- (i) Fivefold disclinations appear on the boundary and move into the internal area.
- (ii) The number of excess fivefold disclinations in the internal area is almost constant, but the shape gradually

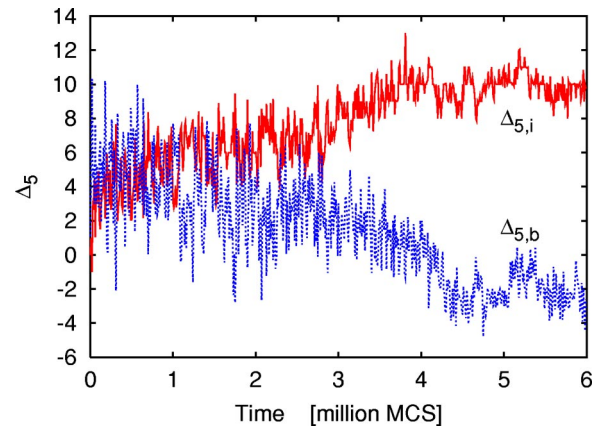


FIG. 17. (Color online) Time dependence of excess fivefold coordinated vertices  $\Delta_{5,i}$  in the internal area (full line) and  $\Delta_{5,b}$  at the domain boundary (dotted line) for  $N_A=368$ ,  $\ell_A=1.50$ ,  $\lambda=2.0$ , and  $C_0^A=0.2$ . See Fig. 15 for the corresponding configurations.

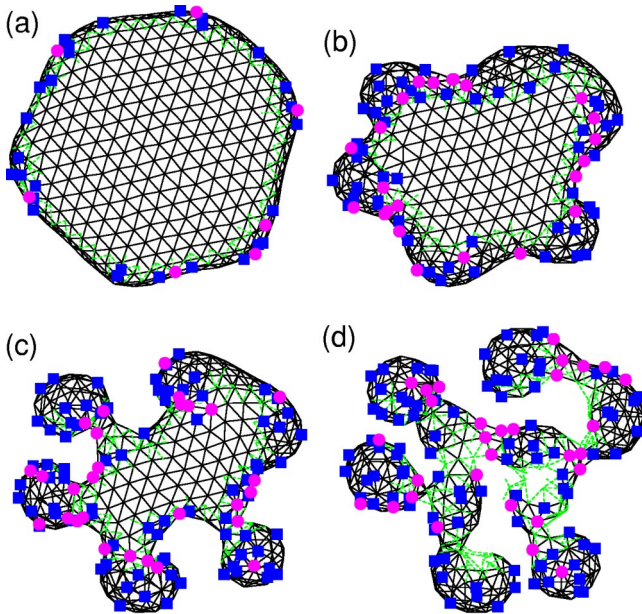


FIG. 18. (Color online) Snapshots of configurations during the budding process after a quench from an initial spherical state for large spontaneous curvature  $C_0^A \sqrt{N_A} \gg 1$ . The pictures show a top view of the crystalline domain; the fluid part of the membrane is not shown. Fivefold and sevenfold coordinated vertices are marked by squares and circles, respectively. The parameters are  $N_A = 368$ ,  $\ell_A = 1.435$ ,  $\lambda = 1.50$ , and  $C_0^A = 1.0$ . Snapshots are shown at time (a)  $t = 0.03 \times 10^6$ , (b)  $t = 0.06 \times 10^6$ , (c)  $t = 0.07 \times 10^6$ , and (d)  $t = 0.1 \times 10^6$  Monte Carlo steps after the quench.

changes until it becomes a half sphere. The boundary length is decreasing roughly linearly with time.

(iii) The half sphere quickly changes to a bud with a narrow neck. The boundary length is again decreasing linearly, but with a considerably larger slope than in regimes (i) and (ii).

(iv) The final budded state is reached.

Note the similarity of the configurations shown in Fig. 15 with the rounded clathrin-coated pits in Fig. 1.

### B. Microcages

We can also consider the case of a quench to a state of large spontaneous curvature  $C_0^A R_A \gg 1$ , and very small line tension. The budding process now proceeds very differently, in particular for a large Young modulus (smaller tether length). This can be seen in the sequence of snapshots given in Fig. 18, where small buds are forming near the domain boundary, while the central region of the domain remains essentially flat.

The shape of the clathrin domain now evolves as follows.

(i) At the beginning, the interior part of the domain remains flat, since no defects are present. The mobility of defects is low for large Young modulus. Therefore, only the boundary region can curve, which it does. The domain shape becomes a flattened mushroom.

(ii) A wavelike instability occurs at the boundary, which leads to the formation of many small, spherical buds. This is possible because the line tension is very small. This state

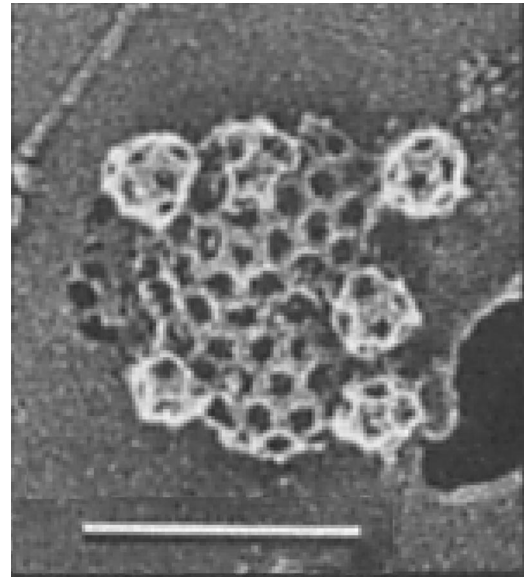


FIG. 19. Clathrin network with nucleated microcages in chick cells acidified by nigericin treatment at pH 6.3 for 5 min at 37 °C. The nucleated microcages do not contain plasma membrane. Bar, 0.2  $\mu\text{m}$ . Reproduced from Ref. [14] by copyright permission of The Rockefeller University Press.

strongly resembles the microcages seen in clathrin domains after a strong quench in pH (see Fig. 19).

(iii) The state of small buds is not stable, but evolves into a cylindrical shape with time. The cylindrical structures elongate, and the whole clathrin domain is composed of several cylindrical structures, which include fluid vertices in some parts.

(iv) After a long time, several isolated clathrin caps float on the fluid membrane.

### VII. BUDDING OF CLATHRIN-COATED MEMBRANES

The biochemistry of the budding process in clathrin-coated vesicles has been studied in considerable detail in recent years [44–46]. In addition to clathrin, many other proteins have been found to play an important role in clathrin-mediated endocytosis. In synaptic vesicle endocytosis, coat proteins AP2 and AP180 are recruited to the membrane to bind the clathrin proteins to the membrane [47]. The invagination of the coated membrane depends on endophilin [48]. Narrowing of the neck region may involve several factors, including actin, intersectin, dynamin, and amphiphysin [49]. Finally, fission depends on dynamin, probably in cooperation with other proteins such as amphiphysin and endophilin [48].

For the comparison of our results with the formation of clathrin-coated vesicles, it is interesting to determine possible mechanisms for the generation of spontaneous curvature. Here, endophilin I seems to play an essential role. It has been shown, for example, that in the absence of endophilin I, the clathrin-coated pit does not transform into a complete bud [48]. It therefore seems natural to assume that endophilin induces a spontaneous curvature in the clathrin domain. This view is supported by the fact that after presynaptic mi-

croinjection of antiendophilin antibodies, the invagination process appears to be inhibited in a concentration-dependent manner, as the depth of the coated pits decreases with increasing antibody concentration [48]. Furthermore, endophilin I has been found to convert lysophosphatic acid, an inverted-cone-shaped lipid, to phosphatic acid, a cone-shaped lipid in the cytoplasmic leaflet of the bilayer [50]. In the interior of the clathrin domain, such a conversion would imply a spontaneous curvature toward the clathrin side, i.e., a negative rather than the desired positive spontaneous curvature. However, the latter activity may occur only in the neck region due to the interaction with dynamin, which forms a ring around the neck. It has been proposed that this induces a negative membrane curvature at the edges of a coated pit, which promotes membrane fission [50].

It has also been shown that clathrin-coated buds morphologically similar to the corresponding structures observed in synaptic vesicles can be generated on protein-free liposomes by incubation with cytosol [51], which suggests that the primary function of membrane proteins is to act as regulators of coat assembly. Furthermore, Heuser [14] has shown that both the *in vivo* acidification of cells as well the *in vitro* acidification of exposed clathrin lattices leads to the formation of budded microcages which nucleate at the edges of the clathrin network (see Fig. 19). The resulting structures are very similar to those shown in Fig. 18 which develop after a quench from an initially flat state for large spontaneous curvature. The microcages observed by Heuser [14] are spherical in shape, with radii on the order of 25–30 nm, and are small compared to normal coated clathrin pits (compare Fig. 1).

### VIII. SUMMARY AND CONCLUSIONS

Heuser [14] suggested that the driving force for the formation of clathrin-coated vesicles is the chemical asymmetry of the clathrin network. This asymmetry induces a finite mean curvature in the membrane which depends on the pH and other environmental conditions. Budding occurs when the curvature becomes sufficiently large. In the model considered in this paper, this asymmetry is described by the spontaneous curvature. We have shown that for a large range of material parameters, budding in crystalline networks of radius  $R_A$  occurs at a critical value of the spontaneous curvature that is a monotonically decreasing function of  $R_A$ . It was also shown that the disclinations required to form the budded state are created at the boundary of the crystalline patch. Budding occurs when a sufficient number of the required fivefold disclinations have been formed and have diffused into the domain interior. For the model parameters we considered, the energies associated with changes in the local structure of the network are of the order of  $k_B T$ .

This scenario is quite different from that suggested by

Mashl and Bruinsma [16]. In particular, the dynamical behavior we observe is not consistent with their type of interior-acquisition model. While Mashl and Bruinsma predict that the formation of fivefold disclinations proceeds via the unbinding of dislocations in the interior region of the network, we have found, as summarized in the last paragraph, that disclinations are formed at the domain boundary before diffusing into the interior.

Furthermore, Mashl and Bruinsma [16] argue that the (20–30)  $k_B T$  of energy required for the dissociation of clathrin coats provides an estimate for the energy needed to break the bond between the four clathrin arms in a polygonal edge. This would imply that diffusive motion of fivefold and sevenfold disclinations induced by thermal fluctuations is rather unlikely. It is still an open question if this is indeed the case. A recent analysis of the size distribution of reconstituted clathrin cages suggests that the relevant energy scale for changes in the local structure of clathrin coats is on the order of  $k_B T$  [52]. Our present Monte Carlo simulations cover the range of small bond energies, while our scaling results should be applicable also for large bond energies.

The detailed behavior at the budding transition depends on the value of the ratio  $Q \equiv K_0 R_A^2 / \kappa$ , the buckling radius of a dislocation, and the distance from the two-dimensional melting transition. The various scenarios are discussed in Sec. IV and summarized in Fig. 14. For the current simulations,  $Q \approx 400$ , so that the transition occurs in the crossover region from the crystalline to the hexatic phase. In this case, the buckling radius is on the order of the domain size, the stretching energy is comparable to the bending energy, and short grain boundaries can be seen at the topologically required fivefold disclinations.

It remains a formidable challenge to elucidate the various mechanisms involved in clathrin-mediated endocytosis in living cells. For this reason, it would be extremely interesting to perform further studies on the endocytosis of protein-free liposomes in order to determine the extent to which simple models of the type discussed in this paper can describe the generic features of formation of clathrin-coated pits. Experiments on simple, well characterized systems could be used in conjunction with simulations, as was done in Ref. [19] for giant synthetic lipid bilayer vesicles, to quantify our understanding of the underlying physical mechanism of the budding of coated pits.

### ACKNOWLEDGMENTS

TK thanks the Japanese Ministry of Education, Science and Culture for financial support during a visit to the Research Center Jülich. D.M.K. acknowledges support from the National Science Foundation under Grant No. DMR-0083219 and the donors of The Petroleum Research Fund, administered by the ACS.

- 
- [1] H. M. McConnell, *Annu. Rev. Phys. Chem.* **42**, 171 (1991).  
 [2] S. L. Keller, W. H. Pitcher III, W. H. Huestis, and H. M. McConnell, *Phys. Rev. Lett.* **81**, 5019 (1998).  
 [3] P. F. F. Almeida, W. L. C. Vaz, and T. E. Thompson, *Biochem-*

*istry* **31**, 6739 (1992).

- [4] J. Korlach, P. Schwille, W. W. Webb, and G. W. Feigensohn, *Proc. Natl. Acad. Sci. U.S.A.* **96**, 8461 (1999).  
 [5] P. Ratanabangkoorn *et al.*, *Langmuir* **18**, 4270 (2002).

- [6] S. L. Veatch and S. L. Keller, *Phys. Rev. Lett.* **89**, 268101 (2002).
- [7] T. Baumgart, S. T. Hess, G. W. Feigenson, and W. W. Webb *Nature (London)* **425**, 821 (2003).
- [8] R. Lipowsky, *J. Phys. II* **2**, 1825 (1992).
- [9] R. Lipowsky, *Biophys. J.* **64**, 1133 (1993).
- [10] C. Dietrich *et al.*, *Biophys. J.* **80**, 1417 (2001).
- [11] B. Alberts *et al.*, *Molecular Biology of the Cell*, 2nd ed. (Garland, New York, 1989).
- [12] J. Heuser and L. Evans, *J. Cell Biol.* **84**, 560 (1980).
- [13] J. Heuser *et al.*, *J. Cell Biol.* **105**, 1999 (1987).
- [14] J. Heuser, *J. Cell Biol.* **108**, 401 (1989).
- [15] A. J. Jin and R. Nossal, *Biophys. J.* **65**, 1523 (1993).
- [16] R. J. Mashl and R. F. Bruinsma, *Biophys. J.* **74**, 2862 (1998).
- [17] G. Gompper and D. M. Kroll, *J. Phys.: Condens. Matter* **9**, 8795 (1997).
- [18] G. Gompper and D. M. Kroll, *Phys. Rev. E* **51**, 514 (1995).
- [19] H.-G. Döbereiner *et al.*, *Phys. Rev. Lett.* **91**, 048301 (2003).
- [20] G. Gompper and D. M. Kroll, *Phys. Rev. E* **52**, 4198 (1995).
- [21] P. B. S. Kumar, G. Gompper, and R. Lipowsky, *Phys. Rev. Lett.* **86**, 3911 (2001).
- [22] G. Gompper and D. M. Kroll, *Eur. Phys. J. E* **1**, 153 (2000).
- [23] G. Gompper and D. M. Kroll, *Europhys. Lett.* **58**, 60 (2002).
- [24] G. Gompper and D. M. Kroll, *Phys. Rev. Lett.* **78**, 2859 (1997).
- [25] G. Gompper and D. M. Kroll, *J. Phys. I* **7**, 1369 (1997).
- [26] D. R. Nelson, in *Phase Transitions and Critical Phenomena*, edited by C. Domb and J. Lebowitz (Academic Press, London, 1983), Vol. 7, pp.1–99.
- [27] W. Helfrich, *Z. Naturforsch. C* **C28c**, 693 (1973).
- [28] C. Itzykson, in *Proceedings of the GIFT Seminar, Jaca 85*, edited by J. Abad, M. Asorey, and A. Cruz (World Scientific, Singapore, 1986), pp.130–188.
- [29] G. Gompper and D. M. Kroll, *J. Phys. I* **6**, 1305 (1996).
- [30] P. B. S. Kumar and M. Rao, *Mol. Cryst. Liq. Cryst. Sci. Technol., Sect. A* **288**, 105 (1996).
- [31] P. B. S. Kumar and M. Rao, *Phys. Rev. Lett.* **80**, 2489 (1998).
- [32] F. Jülicher and R. Lipowsky, *Phys. Rev. E* **53**, 2670 (1996).
- [33] F. Jülicher and R. Lipowsky, *Phys. Rev. Lett.* **70**, 2964 (1993).
- [34] H. S. Seung and D. R. Nelson, *Phys. Rev. A* **38**, 1005 (1988).
- [35] M. J. Bowick, D. R. Nelson, and A. Travesset, *Phys. Rev. B* **62**, 8738 (2001).
- [36] T. A. Witten and H. Li, *Europhys. Lett.* **23**, 51 (1993).
- [37] A. Lobkovsky *et al.*, *Science* **270**, 1482 (1995).
- [38] Z. Zhang, H. T. Davis, R. S. Maier, and D. M. Kroll, *Phys. Rev. B* **52**, 5404 (1995).
- [39] M. W. Deem and D. R. Nelson, *Phys. Rev. E* **53**, 2551 (1996).
- [40] J.-M. Park and T. C. Lubensky, *J. Phys. I* **6**, 493 (1996).
- [41] J.-M. Park and T. C. Lubensky, *Phys. Rev. E* **53**, 2648 (1996).
- [42] F. David, E. Guitter, and L. Peliti, *J. Phys. (France)* **48**, 2059 (1987).
- [43] The translational entropy of the topological disclinations, which has been omitted in our analytical estimates in Sec. IV, may add another logarithmic contribution to  $\Gamma(R_A)$ . However, this contribution should be smaller than the other terms by at least a factor of  $(k_B T/\kappa)$ , and should therefore make only a small correction to our estimates.
- [44] L. Brodin, P. Löw, and O. Shupliakov, *Curr. Opin. Neurobiol.* **10**, 312 (2000).
- [45] B. M. F. Pearse, C. J. Smith, and D. J. Owen, *Curr. Opin. Struct. Biol.* **10**, 220 (2000).
- [46] E. D. Gundelfinger, M. M. Kessels, and B. Qualmann, *Nat. Rev. Mol. Cell Biol.* **4**, 127 (2003).
- [47] V. Haucke and P. De Camilli, *Science* **285**, 1268 (1999).
- [48] N. Ringstad *et al.*, *Neuron* **24**, 143 (1999).
- [49] K. Takei, V. Slepnev, and P. De Camilli, *Nat. Cell Biol.* **1**, 33 (1999).
- [50] A. Schmidt *et al.*, *Nature (London)* **401**, 133 (1999).
- [51] K. Takei *et al.*, *Cell* **94**, 131 (1998).
- [52] R. Nossal, *Traffic* **2**, 138 (2001).